A Versatile Noise Performance Metric for Electrical Impedance Tomography Algorithms

Fabian Braun*, Martin Proença, Josep Solà, Jean-Philippe Thiran, and Andy Adler

***Abstract*—Electrical impedance tomography (EIT) is an emerging technology for real-time monitoring of patients under mechanical ventilation. EIT has the potential to offer continuous medical monitoring while being noninvasive, radiation free, and low cost. Due to their ill-posedness, image reconstruction typically uses regularization, which implies a hyperparameter controlling the tradeoff between noise rejection and resolution or other accuracies. In order to compare reconstruction algorithms, it is common to choose hyperparameter values such that the reconstructed images have equal noise performance (NP), i.e., the amount of measurement noise reflected in the images. For EIT many methods have been suggested, but none work well when the data originate from different measurement setups, such as for different electrode positions or measurement patterns. To address this issue, we propose a new NP metric based on the average signal-to-noise ratio in the image domain. The approach is validated for EIT using simulation experiments on a human thorax model and measurements on a resistor phantom. Results show that the approach is robust to the measurement configuration (i.e., number and position of electrodes, skip pattern) and the reconstruction algorithm used. We propose this novel approach as a way to select optimized measurement configurations and algorithms.**

***Index Terms*—Cross validation, EIT, hyperparameter selection, L-curve, noise figure, noise performance, SNR.**

I. Introduction

MECHANICAL ventilation provides life-saving support for patients in intensive care units, but – if not applied properly – can also lead to severe complications. Those can be reduced by continuous monitoring of regional ventilation at the bedside, as recently made possible with electrical impedance tomography (EIT) [1], a radiation-free medical imaging modality [2]. Apart from ventilation, chest EIT has also been suggested for assessing haemodynamics such as pulmonary perfusion, stroke volume or blood pressure [3].

EIT uses current stimulation and voltage measurements at body surface electrodes to reconstruct tomographic images, which represent an estimate of a body's internal electrical conductivity. In EIT and other soft field tomographies, the physics of the probing energy is diffusive, resulting in wide variations of sensitivity across the body, i.e. EIT is much more sensitive to conductivity changes near its electrodes than to changes deeper in the body. Consequently, the reconstruction formulation is ill-conditioned. For a given finite element model of the body, sensitivity is typically represented as a Jacobian matrix, $\boldsymbol{J}$, where the (i,j)th element $\boldsymbol{J}_{i,j} = \partial F_i(\boldsymbol{m})/\partial \boldsymbol{m}_j$, is the sensitivity of the ith surface voltage measurement $\boldsymbol{v}_i = F_i(\boldsymbol{m})$ to a conductivity change in the jth model element $\boldsymbol{m}_j$. The operator $F(\cdot)$ represents the forward model transforming the conductivity distribution $\boldsymbol{m}$ into a surface voltage measurement $\boldsymbol{v}$. The large sensitivity variations of EIT is reflected in an ill-conditioned $\boldsymbol{J}$ [2].

Reconstruction of such tomographic images uses inverse problem techniques, which introduce additional constraints to stabilize the estimated images, and to make them more robust to interference and noise [2], [4]. Regularized algorithms estimate a conductivity distribution $\hat{\boldsymbol{m}} = R(\boldsymbol{v}, \lambda)$ using algorithm $R(\cdot,\cdot)$ with data $\boldsymbol{v}$ and hyperparameter λ. In particular, Tikhonov-type regularization seeks an estimate, $\hat{\boldsymbol{m}}$, which minimizes the norm $\|\boldsymbol{v} - F(\hat{\boldsymbol{m}})\| + \lambda P(\hat{\boldsymbol{m}})$, where $P(\cdot)$ is a function which penalizes noisy images. Such regularization implies an impact on various measures of image accuracy, such as resolution. Most regularized schemes define a hyperparameter (here λ) which controls the amount of regularization, and can be seen as a trade-off parameter between image robustness and accuracy. In many cases, this choice can be described as a "resolution-noise performance trade-off".

In using regularization techniques, a key decision is the selection of an appropriate (or "best") value of the hyperparameter λ. From the various λ selection approaches which have been proposed [5], [6], we review three commonly used in EIT. A key challenge with all these approaches is that they work within a given measurement configuration (electrode number and position, and stimulation and measurement pattern). They thus offer little guidance in scenarios in which measurement

Manuscript received October 23, 2016; revised December 23, 2016; accepted January 22, 2017. Date of publication January 26, 2017; date of current version September 18, 2017. This work was supported in part by the SNSF/Nano-Tera Project OBESENSE (20NA21-1430801) and in part by the Swiss National Science Foundation under Grant 205321-153364/1. *Asterisk indicates corresponding author.*

*F. Braun is with the Systems Division, Centre Suisse d'Electronique et de Microtechnique, Neuchâtel 2002, Switzerland, and also with the Signal Processing Laboratory, Ecole Polytechnique Fédérale de Lausanne, Lausanne 1015, Switzerland (e-mail: fbn@csem.ch).

M. Proença is with the Systems Division, Centre Suisse d'Electronique et de Microtechnique, and also with the Signal Processing Laboratory, Ecole Polytechnique Fédérale de Lausanne.

J Solà is with the Systems Division, Swiss Center for Electronics and Microtechnology.

J. P. Thiran is with the Signal Processing Laboratory, Ecole Polytechnique Fédérale de Lausanne, and also with the Department of Radiology, University Hospital Center and University of Lausanne.

A. Adler is with the Systems and Computer Engineering, Carleton University.

Digital Object Identifier 10.1109/TBME.2017.2659540

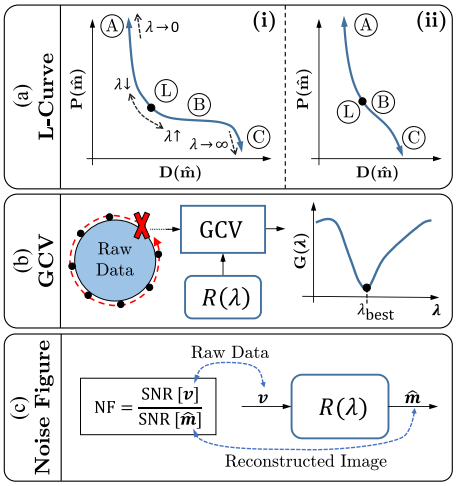

Fig. 1. Three hyperparameter selection approaches commonly used in EIT: (a) L-curve with (i) a classical form and (ii) a form often observed for higher data noise; (b) generalized cross-validation (GCV); (c) noise figure (NF).

configurations need to be compared, for example when optimizing an EIT configuration for a specific experimental or clinical application. To address this requirement, this paper proposes and evaluates a novel noise performance metric.

A. State of the Art in Hyperparameter Selection

We review three state-of-the-art techniques to select regularization hyperparameters.

The most widely cited is the L-curve technique, proposed by Hansen [7]. It is based on finding a best compromise between the data mismatch, $D(\hat{\boldsymbol{m}}) = \|\boldsymbol{v} - F(\hat{\boldsymbol{m}})\|$ and the regularization penalty $P(\hat{\boldsymbol{m}})$. The classical form of the L-curve is shown in Fig. 1(a)-i; values are obtained by calculating the solution over the full range of λ values and plotting each point. Point L is the L-curve point, which represents "best" compromise between $D(\cdot)$ and $P(\cdot)$, in the sense that changes in λ from L increase one penalty without improving the other (L can be precisely defined in terms of the curvature). In region A, as $\lambda \to 0$, the image becomes increasingly noisy, and $P(\cdot)$ increases without significant improvement in $D(\cdot)$. Conversely, in region B, as λ increases, $D(\cdot)$ increases without significant improvement in $P(\cdot)$. Finally, for large λ, the best choice is simply to choose the values which minimizes $P(\cdot)$ without considering the data at all (region C). Thus, the L-curve can be thought of as having a "chair" shape. While the L region is well defined when the noise levels are low, in many applications with higher data noise the curve appears more like Fig. 1(a)-ii, and point L can be difficult to calculate robustly [5].

Another approach is to use a cross-validation scheme, such as generalized cross validation (GCV) [8]. These are motivated by searching for a solution which is best able to predict measured values. The concept of GCV is illustrated in Fig. 1(b). A solution is calculated without each data value in turn, and the prediction error due to each missing data value is then evaluated. The best λ predicts data with the lowest cross-validation error, represented by the minimum of the GCV-function $G(\lambda)$. GCV estimates have not seen much use in EIT; a common claim has been that the GCV tends to underestimate λ, i.e. to provide under-regularized solutions [5].

The third approach, the noise figure (NF), is illustrated in Fig. 1(c). It is defined as the ratio of signal-to-noise ratio (SNR) of the input (raw data $\boldsymbol{v}$) to that of the output (reconstructed image $\hat{\boldsymbol{m}}$) [9]; $\mathrm{NF} = \mathrm{SNR}[\boldsymbol{v}]/\mathrm{SNR}[\hat{\boldsymbol{m}}]$. Here, SNR is defined in terms of image amplitude rather than energy, as $\mathrm{SNR}[\boldsymbol{x}] = \mathrm{mean}[\boldsymbol{x}]/\mathrm{std}[\boldsymbol{x}]$. NF is a useful parameter to compare algorithms using the same measurement configuration (for example, to compare to the original Sheffield backprojection algorithm, an EIT algorithm is recommended to have $\mathrm{NF} = 0.5$ [10]). Limitations of the NF are mentioned at the end of the next section.

B. Practical Aspects and Limitations of the State of the Art

A common limitation associated with the L-curve, GCV and other approaches from the mathematical inverse problem literature is that the optimal λ is defined for each data measurement. From an engineering point of view this is not practical. Instead, the value would be set either when an algorithm or system is designed or manufactured, or perhaps when a system is tuned for a specific application. Thus λ should be best for an expected range of data, rather than for one specific set of measurements. Another consideration is that in practice, a "best" algorithm is defined in terms of user-level performance parameters, such as SNR, resolution, position accuracy (e.g. [10]). It is not clear how, for example, the L-curve optimal point relates to the user-level performance. One further application requirement is the need to compare the performance of different measurement system configurations. If we wish to compare different hardware settings, electrode placements, or stimulation and measurement patterns, then the measured data will necessarily differ. It is not possible to simply use the same numeric value of λ between the different configurations. In order for the comparison between the configurations to be meaningful, the setting of a given performance parameter must be the same, so that other figures of merit can be compared fairly. Most commonly, this means setting approaches to have equal noise performance (NP), i.e. the amount of measurement noise (present at the input) reflected in the images (the output of reconstruction).

One common parameter of this type has been the NF. Unfortunately, as shown later in the present work, NF does not work well for the comparison of different measurement configurations , such as for example a larger skip (separation between stimulation and measurement electrodes).

C. Proposed Approach

We are faced with the challenge of defining a hyperparameter selection strategy which is appropriate for: 1) choosing a suitable λ for a measurement system and a given application, and 2) fairly comparing different systems or different configurations of the same system. In the present work we primarily focus on 2) driven by the motivation of possible scenarios encountered in practice: having a 32 electrode EIT system with the capability to

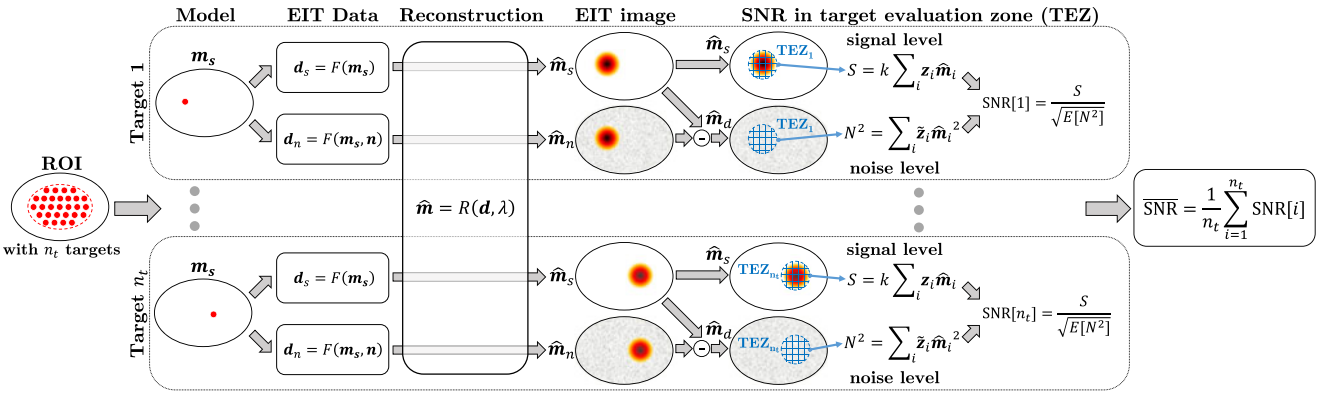

Fig. 2. Block diagram of the proposed framework evaluating the signal-to-noise ratio (SNR) of n_t likely conductivity targets leading to the averaged $\overline{\text{SNR}}$.

use different stimulation and measurement patterns, we would like to know which one is the best pattern e.g. to image the lungs or the heart. In a next step, we might want to compare the performance of the first device to a second device with only 16 electrodes. Once an equal NP is established for all algorithms of these diverse configurations, the image quality can be compared in terms of resolution, position errors, or other figures of merit.

To this end we develop a NP metric called $\overline{\text{SNR}}$ which describes the expected image noise. This noise parameter is calculated for a given measurement system configuration which is defined to include: the stimulation and measurement patterns and the electrode positions.

D. Image Reconstruction for Difference EIT

In this paper we focus on difference EIT, as typically used in clinical applications for stability reasons. In difference EIT a reference voltage $\boldsymbol{v}_r$ is subtracted from the voltage measurement $\boldsymbol{v}$ yielding the difference data $\boldsymbol{d}$. The result of reconstruction $\hat{\boldsymbol{m}}$ thus represents the change in conductivity relative to a reference state. For small changes in conductivity the problem may be linearised as follows:

$$\hat{\boldsymbol{m}} = \boldsymbol{R}(\lambda)\boldsymbol{d} = \boldsymbol{R}(\lambda)(\boldsymbol{v} - \boldsymbol{v}_r) \tag{1}$$

where $\boldsymbol{R}(\lambda)$ represents the reconstruction matrix which depends on the hyperparameter λ. Such linearised one-step difference algorithms are commonly used in clinical EIT and many approaches exist to derive $\boldsymbol{R}(\lambda)$.

This paper is structured as follows: In the methods section we first present the $\overline{\text{SNR}}$ approach from the theory to its implementation. Then, we describe the simulation and practical experiments performed to validate our approach. In the results, we compare the state of the art (L-curve, GCV, NF) to the proposed method. In the discussion we consider some additional observations of this work, followed by a conclusion.

II. Methods

A. $\overline{SNR}$ Framework

We first explain the general concept of the proposed $\overline{\text{SNR}}$ approach in Section II-A1. Then we present its specific solution for linearised one-step reconstruction (Section II-A2), followed by its algorithmic implementation (Section II-A3).

1) General Concept: The suggested $\overline{\text{SNR}}$ measures the average signal-to-noise ratio in the image domain for several objects of interest – hereafter referred to as *targets*. To do so the signal strength of each target is compared to the amount of noise present in the images within the vicinity of each target. Algorithms with equal $\overline{\text{SNR}}$ are thus defined to have equal noise performance (NP).

As illustrated in Fig. 2 we evaluate the individual SNRs from n_t likely targets distributed inside a given region of interest (ROI) of our model. The approach requires a model of likely noise $\boldsymbol{n}$, which is incorporated into the difference EIT data ($\boldsymbol{d} = F(\boldsymbol{m}, \boldsymbol{n})$) prior to reconstruction ($\hat{\boldsymbol{m}} = R(\boldsymbol{d}, \lambda)$). $F(\cdot,\cdot)$ represents the forward model transforming the conductivity change $\boldsymbol{m}$ into the (noisy) difference voltage $\boldsymbol{d}$, and $R(\cdot,\cdot)$ the reconstruction of $\boldsymbol{d}$ into the EIT image $\hat{\boldsymbol{m}}$ (i.e. the estimated conductivity change) while being controlled by the hyperparameter λ. For each of the n_t targets, we estimate the expected signal and noise level in a target-specific evaluation zone (TEZ). To this end, within the TEZ of a given target, we compute the signal level S as the average of a noise-free image $\hat{\boldsymbol{m}}_s$ and the noise level N as the expected root mean square (RMS) amplitude of a pure noise image $\hat{\boldsymbol{m}}_d$. By design, the signal level estimation should be independent of both the spatial resolution (i.e. amount of blurring), and the possible position errors of the reconstruction. Thus, the TEZ is adapted to each target, and is defined as the pixels which exceed one-fourth of the maximum amplitude of $\hat{\boldsymbol{m}}_s$, as suggested by [10]; the TEZ thus includes most of the visually significant image contributions. In this way, the estimate S always captures a comparable portion of the target response in $\hat{\boldsymbol{m}}_s$, independent of the spatial resolution of the reconstruction. The signal estimate S is further scaled with a factor $k = V_{\text{TEZ}}/V_t$ which corrects for the ratio of blurring, i.e. the size of the target response in the image domain V_{TEZ} versus the effective target size V_t. This correction factor k makes the signal estimate independent of the spatial resolution of reconstruction (i.e. size of the TEZ) and the size of the target and thus allows a fair comparison between estimates of different targets and/or algorithms.

The final NP metric $\overline{\mathrm{SNR}}$ is expressed as the average SNR of all n_t targets which leads to the generalized equation:

$$\overline{\mathrm{SNR}} = \mathrm{E}_t \left[\frac{k \sum_{i=1}^{n_p} [\boldsymbol{z}]_i [\hat{\boldsymbol{m}}_s]_i}{\sqrt{\mathrm{E}_n \left[\sum_{i=1}^{n_p} [\boldsymbol{z}]_i [\hat{\boldsymbol{m}}_d]_i^2 \right]}} \right] \tag{2}$$

where $\mathrm{E}_n[\cdot]$ denotes the expected value of the noise model (stochastic domain) and $\mathrm{E}_t[\cdot]$ the expected value calculated over the finite set of n_t targets. The target-specific vector $\boldsymbol{z}$ weighing each of the n_p image elements by its area times its contribution to the TEZ (i.e. $z_i = 0$ if image element i is outside the TEZ) is further defined in the next section.

As mentioned before, most clinical EIT applications use one-step linearised reconstruction. We therefore focus on this type of reconstruction and present a particular solution for (2) hereafter.

2) Solution for Linearised Reconstruction: When using a linear model and assuming $\boldsymbol{n}$ as additive noise (characterized by a covariance $\boldsymbol{\Sigma}_n$), we have $\boldsymbol{d}_s = \boldsymbol{J}\boldsymbol{m}_s$, and $\boldsymbol{d}_n = \boldsymbol{J}\boldsymbol{m}_s + \boldsymbol{n}$, where $\boldsymbol{d}_s, \boldsymbol{d}_n \in \mathbb{R}^{n_d}$ are the difference EIT measurements and $\boldsymbol{J} \in \mathbb{R}^{n_d \times n_e}$ is the Jacobian matrix (with n_d as the number of EIT voltage measurements and n_e the number of finite elements in the forward model). The two images of interest, $\hat{\boldsymbol{m}}_s, \hat{\boldsymbol{m}}_d$ are thus calculated using (1):

$$\hat{\boldsymbol{m}}_s = \boldsymbol{R}\boldsymbol{d}_s = \boldsymbol{R}\boldsymbol{J}\boldsymbol{m}_s \tag{3}$$

$$\hat{\boldsymbol{m}}_d = \boldsymbol{R}(\boldsymbol{d}_s - \boldsymbol{d}_n) = \boldsymbol{R}\boldsymbol{n}. \tag{4}$$

From these images we estimate the signal level S from $\hat{\boldsymbol{m}}_s$ and noise level N from $\hat{\boldsymbol{m}}_d$, with the analysis being restricted to the TEZ. To this end, we make use of the normalized weighting vector $\boldsymbol{z} \in \mathbb{R}^{n_p}$ which contains, for each image element i (e.g. pixel), its area a_i multiplied by a binary number c_i (equals 0/1 if outside/inside the TEZ), yielding $z_i \propto a_i c_i$, with $\sum z_i = 1$. For the sake of simplicity, the following equations are limited to one single target but extended to multiple targets at the end of this section. The signal level S is defined as the average of $\hat{\boldsymbol{m}}_s$ within the TEZ:

$$\mathrm{S} = k \sum_{i=1}^{n_p} [\boldsymbol{z}]_i [\hat{\boldsymbol{m}}_s]_i = k\, \boldsymbol{z}^t \hat{\boldsymbol{m}}_s = \tilde{\boldsymbol{z}}^t \boldsymbol{R}\boldsymbol{J}\boldsymbol{m}_s, \tag{5}$$

where $\tilde{\boldsymbol{z}} = k\boldsymbol{z} = (V_{\mathrm{TEZ}}/V_t)\boldsymbol{z}$ with $V_{\mathrm{TEZ}} = \sum a_i c_i$, i.e. the total area of all image elements within the TEZ, and V_t the volume of the conductivity target. The squared noise level N^2 is defined as the weighted mean square amplitude of $\hat{\boldsymbol{m}}_d$:

$$\mathrm{E}\left[\mathrm{N}^2\right] = \mathrm{E}\left[\sum_{i=1}^{n_p} [\boldsymbol{z}]_i [\hat{\boldsymbol{m}}_d]_i^2 \right] = \mathrm{E}\left[||\boldsymbol{D}\hat{\boldsymbol{m}}_d||^2 \right] \tag{6}$$

where $\boldsymbol{D}$ is a diagonal matrix with $[\boldsymbol{D}]_{ii} = \sqrt{z_i}$ yielding:

$$\begin{aligned}
\mathrm{E}\left[\mathrm{N}^2\right] &= \mathrm{E}\left[\mathrm{tr}\left[\boldsymbol{D}\hat{\boldsymbol{m}}_d \hat{\boldsymbol{m}}_d^T \boldsymbol{D}^T \right] \right] = \mathrm{E}\left[\mathrm{tr}\left[\boldsymbol{D}^T \boldsymbol{D}\hat{\boldsymbol{m}}_d \hat{\boldsymbol{m}}_d^T \right] \right] \\
&= \mathrm{E}\left[\sum_{i=1}^{n_p} [\boldsymbol{D}]_{ii}^2 [\hat{\boldsymbol{m}}_d \hat{\boldsymbol{m}}_d^T]_{ii} \right] = \mathrm{E}\left[\sum_{i=1}^{n_p} [\boldsymbol{z}]_i [\hat{\boldsymbol{m}}_d \hat{\boldsymbol{m}}_d^T]_{ii} \right] \\
&= \mathrm{E}\left[\boldsymbol{z}^t \,\mathrm{diag}\left(\hat{\boldsymbol{m}}_d \hat{\boldsymbol{m}}_d^T\right) \right] = \mathrm{E}\left[\boldsymbol{z}^t \,\mathrm{diag}\left(\boldsymbol{R}\boldsymbol{n}\boldsymbol{n}^t \boldsymbol{R}^t\right) \right] \\
&= \boldsymbol{z}^t \,\mathrm{diag}\left(\boldsymbol{R}\boldsymbol{\Sigma}_n \boldsymbol{R}^t\right).
\end{aligned} \tag{7}$$

The choice of calculating the noise from the diagonal entries of $\boldsymbol{R}\boldsymbol{\Sigma}_n\boldsymbol{R}^t$ rather than from the full covariance matrix stems from the fact that we are estimating N as the RMS amplitude along the spatial dimension (i.e. for each image element). If the full covariance matrix were used, noise would be estimated as the RMS amplitude (along the stochastic dimension) of a conductivity change spatially averaged over the TEZ ($\mathrm{E}\left[(\boldsymbol{z}^t\hat{\boldsymbol{m}}_d)^2\right] = \boldsymbol{z}^t\boldsymbol{R}\boldsymbol{\Sigma}_n\boldsymbol{R}^t\boldsymbol{z}$), and would sum over the off-diagonal entries in the covariance matrix. In this case, off-diagonal entries with opposite sign would reduce the estimated noise within the TEZ. This would lead to an overestimated SNR, especially in reconstruction algorithms with high spatial resolution when compared to lower resolution algorithms.

Combining (5) and (7) leads to the SNR of one single target:

$$\mathrm{SNR} = \frac{\mathrm{S}}{\sqrt{\mathrm{N}^2}} = \frac{\tilde{\boldsymbol{z}}^t \boldsymbol{R}\boldsymbol{J}\boldsymbol{m}_s}{\sqrt{\boldsymbol{z}^t \,\mathrm{diag}\left(\boldsymbol{R}\boldsymbol{\Sigma}_n\boldsymbol{R}^t\right)}}. \tag{8}$$

We further extend this to multiple targets with their changes in conductivity $\boldsymbol{M} \in \mathbb{R}^{n_e \times n_t}$ and the corresponding evaluation zones $\boldsymbol{Z}, \tilde{\boldsymbol{Z}} \in \mathbb{R}^{n_p \times n_t}$, where each column in $\boldsymbol{M}$ contains the conductivity change of one target (e.g. $\boldsymbol{m}_s$), $\boldsymbol{Z}$ the TEZ of this target (e.g. $\boldsymbol{z}$) and $\tilde{\boldsymbol{Z}}$ its scaled version (e.g. $\tilde{\boldsymbol{z}}$). This leads a vector of n_t SNRs:

$$\mathbf{SNR} = \mathrm{diag}\left(\tilde{\boldsymbol{Z}}^t \boldsymbol{R}\boldsymbol{J}\boldsymbol{M}\right) \oslash \sqrt{\boldsymbol{Z}^t \,\mathrm{diag}\left(\boldsymbol{R}\boldsymbol{\Sigma}_n\boldsymbol{R}^t\right)} \tag{9}$$

where $\oslash$ denotes the Hadamard division (element-wise division). For uncorrelated and uniform noise, where $\boldsymbol{\Sigma}_n$ is a diagonal matrix with $\boldsymbol{\Sigma}_n = \sigma_n^2 \boldsymbol{I}$, this can be simplified to:

$$\mathbf{SNR} = \mathrm{diag}\left(\tilde{\boldsymbol{Z}}^t \boldsymbol{R}\boldsymbol{J}\boldsymbol{M}\right) \oslash \left(\sigma_n \sqrt{\boldsymbol{Z}^t \,\mathrm{diag}\left(\boldsymbol{R}\boldsymbol{R}^t\right)}\right). \tag{10}$$

The final SNR is then calculated as the mean of all targets $\overline{\mathrm{SNR}} = \frac{1}{n_t}\sum_{i=1}^{n_t}[\mathrm{SNR}]_i$, in order to obtain the average NP inside the ROI. The expressions in (9) and (10) are comparable to the $\mathrm{SNR}_{\mathrm{out}}$ defined by Adler *et al.* [9] but evaluated in a restricted region of the image – the TEZ – and averaged over multiple targets.

3) Algorithm Implementation: For a given application including a model of the likely body shape, the Jacobian $\boldsymbol{J}$ and – provided a given λ – the reconstruction matrix $\boldsymbol{R}(\lambda)$ are known. With (9) and (10) the $\overline{\mathrm{SNR}}$ is then calculated by the following steps.

1) In the region where the conductivity changes of interest are to be observed (ROI) we distribute n_t targets of desired size and amplitude in our model, leading to $\boldsymbol{M}$.

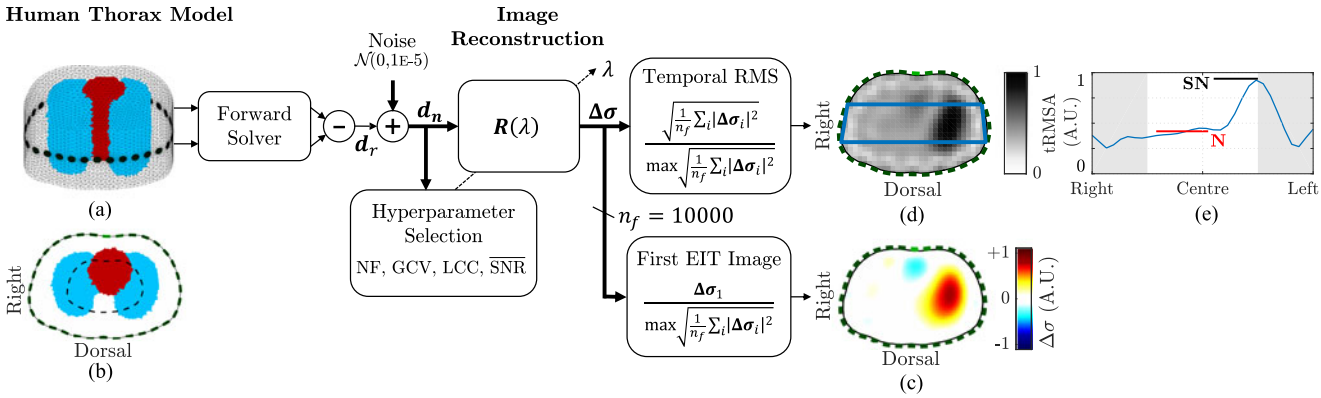

Fig. 3. Overview of the simulation experiments: (a) 3D model of human thorax with lungs (blue) and heart (red) and (b) its corresponding 2D model in medical orientation (with ROI for $\overline{\text{SNR}}$ calculation as dashed black line). The difference voltages $\boldsymbol{d}_r$ obtained after forward solving are affected by n_f realizations of additive white Gaussian noise $\mathcal{N}(0, 1\text{E-}5)$ and then reconstructed to n_f noisy EIT images $\boldsymbol{\Delta\sigma}$. The noise level in the reconstructed images is illustrated by one single noisy EIT image and further analyzed by the temporal root mean square of all noisy EIT images as described in the following. (c) Example EIT image with positive/negative conductivity change in left lung and heart, respectively. The green rectangles depict the EIT electrodes. (d) Pixel-wise, temporal root mean squared amplitude (tRMSA) of the n_f noisy EIT image. This image shows the square root of the signal and noise power. The region delineated in blue is used to generate (e) the tRMSA cross section showing a transversal cut through the tRMSA image with the region outside the ROI shaded grey. It shows the ratio of noise-affected signal level SN (left lung) versus noise level N (right lung) and allows to estimate an approximative SNR $\approx \frac{\text{SN}-\text{N}}{\text{N}}$. In the above example with SN $= 0.94$ and N $= 0.42$ we estimate SNR ≈ 1.24. Note that (c), (d), and (e) are normalized to maximal tRMSA.

2) For each target, we reconstruct an image $\hat{\boldsymbol{m}}_s$ of which we determine the one-fourth amplitude pixels. These pixels define the evaluation zone (TEZ) in the image domain, leading to n_t TEZs contained in $\boldsymbol{Z}$ and $\tilde{\boldsymbol{Z}}$.
3) Depending on the desired noise characteristics we compute **SNR** using (9) or (10) and average to obtain $\overline{\text{SNR}}$.

B. Validation Experiments

To validate the approach proposed, a number of simulation experiments were performed on a human thorax model. To this end, the aforementioned algorithm was implemented in Matlab using the open-source EIT toolbox EIDORS [11] and will be freely available upon its next release. To illustrate the approach on measured data, a commercial EIT system was used to perform measurements on a resistor phantom. Finally, a simulation on an open geometry model was carried out to evaluate the potential of the $\overline{\text{SNR}}$ approach for other fields of EIT such as geophysics.

1) Algorithm Parameters: For the implementation of the proposed method in thoracic EIT applications, we recommend an ROI extending to 50% of the distance from the center of mass to the boundary as illustrated in Fig. 3(b). The therein contained $n_t = 200$ uniformly distributed spherical targets are positioned at the level of the electrodes and have a relative radius r_t of 5% of the medium radius R_m. Moreover, $\overline{\text{SNR}}$ was calculated using (10) with $\sigma_n = 1$. The choice of these parameters is justified in the discussion section.

In order to tune an EIT reconstruction algorithm to a desired $\overline{\text{SNR}}$ i.e. selecting the hyperparameter λ of $\boldsymbol{R}(\lambda)$, a bisection search technique was applied [5].

2) Image Reconstruction: In the present work we use two reconstruction algorithms widely used for thoracic EIT: GREIT with the recommended settings [10] and one-step Gauss-Newton (GN) with a Laplace-prior [2], [4].

3) Simulation Experiments: The simulation experiments are illustrated in Fig. 3 and described hereafter. A 3D extruded model of a human thorax [shown in Fig. 3(a)] was used with realistic conductivities ($\sigma_{\text{Background}} = 0.20$ S/m, $\sigma_{\text{Lungs}} = 0.13$ S/m, $\sigma_{\text{Heart}} = 0.55$ S/m) [12]. A set of representative difference EIT voltages $\boldsymbol{d}_r$ was generated by changing the conductivity of the left lung and the heart by 10% and -5%, respectively. The right lung was left unchanged. An example of a reconstructed EIT image is shown in Fig. 3(c). To mimic a realistic scenario, additive white Gaussian noise $\mathcal{N}(0, 1\text{E-}5)$ was added to the difference data simulated, with which $n_f = 10000$ realizations of a noisy EIT voltages $\boldsymbol{d}_n$ were generated. These EIT data were reconstructed with various algorithms $\boldsymbol{R}(\lambda)$ whose hyperparameter λ was selected based on different strategies: (a) a given $\overline{\text{SNR}}$, (b) a given noise figure (NF) [5], [9], (c) the L-curve criterion (LCC) [7], [13], or (d) the generalized cross-validation (GCV) [13]. The latter two were implemented in EIDORS using Hansen's Regularization Tools [14] and λ was selected as the median value of n_f hyperparameters resulting from applying the LCC or GCV to each of the noisy EIT voltages individually.

Additionally, the reliability of the different hyperparameter selection approaches was investigated for various scenarios by changing (a) the number and (b) position of electrodes, (c) the skip of the bipolar stimulation pattern (number of inactive electrodes in between the two ones actively measuring voltage/injecting current), (d) the image resolution (i.e. number of pixels) or (e) the reconstruction algorithm (GREIT or GN). Unless otherwise noted, per default, data from 16 equidistantly spaced electrodes and bipolar stimulation with skip 0 (*adjacent* stimulation pattern) were reconstructed using GN onto an image of 32×32 pixels.

For each of the scenarios simulated the NP is analysed visually, either on the so-called temporal RMS amplitude (tRMSA)

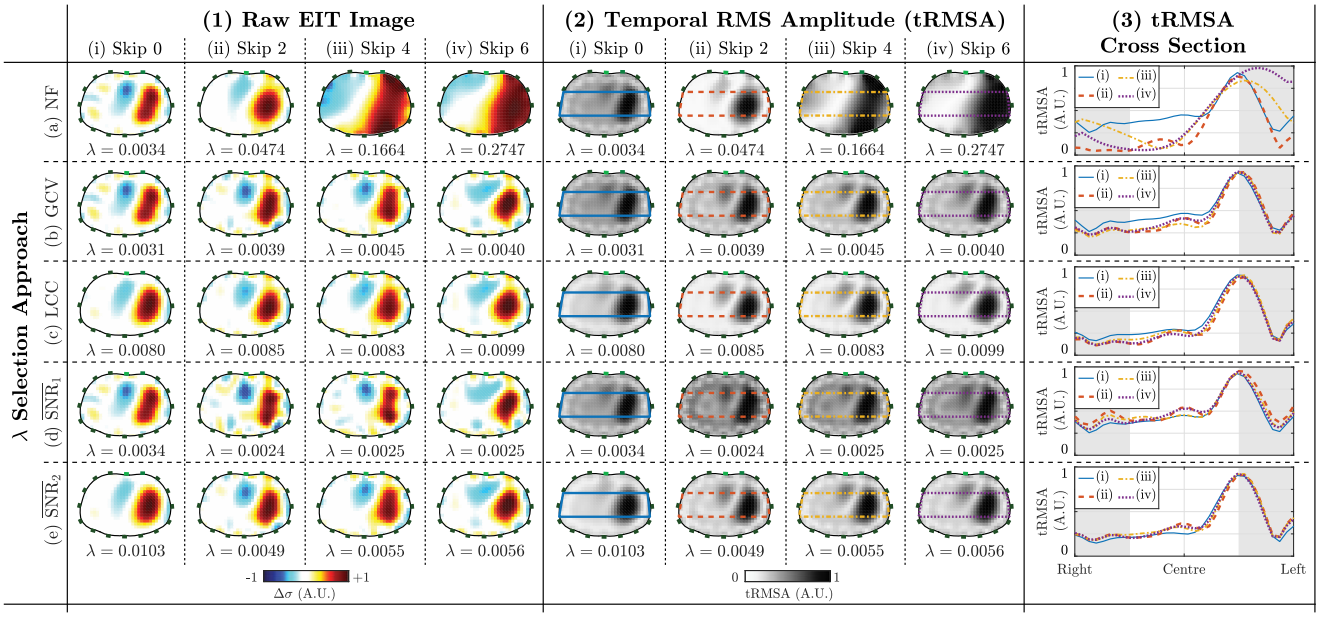

Fig. 4. Noise performance of GN reconstructions for four examples of skip pattern (i)–(iv), and five approaches for hyperparameter selection, each shown in one row: (a) fixed noise figure (NF $= 0.5$), (b) generalized cross-validation (GCV), (c) L-curve criterion (LCC), (d) fixed $\overline{\text{SNR}}$ of $\overline{\text{SNR}}_1 = 2.20\text{E-}5$ (corresponds to NF $= 0.5$ at skip 0), and (e) fixed $\overline{\text{SNR}}$ of $\overline{\text{SNR}}_2 = 2 \cdot \overline{\text{SNR}}_1 = 4.41\text{E-}5$. For each approach and skip we show (1) one single EIT image (all with identical noise), (2) the temporal RMS amplitude (tRMSA) images, and (3) their cross sections along the transverse axis of the zone delineated in the corresponding tRMSA image. All images are normalized to their maximal tRMS amplitude as described in Fig. 3.

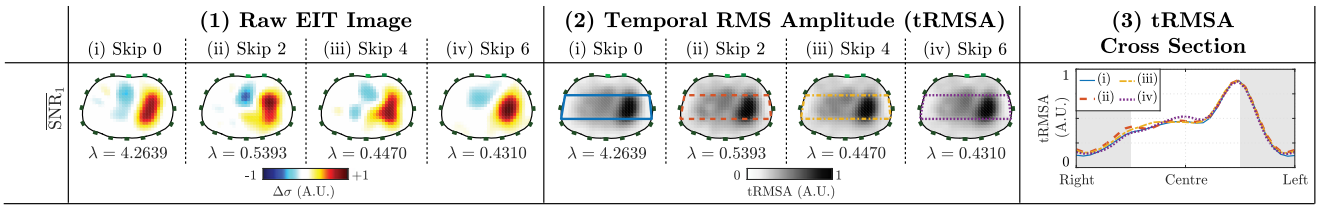

Fig. 5. Noise performance of GREIT reconstructions (with fixed $\overline{\text{SNR}} = 2.20\text{E-}5$) for four examples of skip pattern (i)–(iv). For each skip we show (1) one single EIT image (all with identical noise), (2) the temporal RMS amplitude (tRMSA) images, and (3) their cross sections along the transverse axis of the zone delineated in the corresponding tRMSA image. All images are normalized to their maximal tRMS amplitude as described in Fig. 3.

image or its resulting cross section plot described in the following. The tRMSA image [see Fig. 3(d)] is calculated as the pixel-wise RMS amplitude (in the temporal domain) from the n_f reconstructed noisy EIT images $\boldsymbol{\Delta\sigma}$. The tRMSA image and the corresponding cross section plot Fig. 3(e) show the ratio of noise-affected signal (left lung) vs. noise (right lung) and thus allow a visual analysis of the NP and its spatial distribution as further detailed in Fig. 3.

4) Practical Experiments: In a laboratory experiment a resistor phantom (Swisstom Mesh Phantom 32-HG) was connected to the 32-electrode EIT belt of the Swisstom PioneerSet (Swisstom, Landquart, Switzerland). The mesh phantom contains 160 resistors in a star-like arrangement of which four can be short-circuited by a pushbutton resulting in local conductivity perturbations [15]. The four pushbuttons A, B, C and D are located close to electrode 1, 9, 17 and 25 and lead to a local increase in conductivity at the top, right, bottom or left of the reconstructed image, respectively. Five measurements were performed, each with a different skip pattern: 0, 3, 4, 7 and 8. Data were recorded using the Swisstom STEMLab software (Version 2.3.2 rev 749). At the beginning of each measurement four local changes in conductivity were generated by consecutively pressing each of the pushbuttons (A, B, C, D) of the resistor phantom during 5 s. Then the phantom was left untouched while the recording continued for 2.5 min, enabling the estimation of the device-specific noise characteristics.

5) Open Geometry Example: The previous experiments concentrate on the application of thoracic EIT where electrodes are placed on a closed geometry. However, there are other uses of EIT, such as geophysics, where the electrodes can be placed on an open geometry. In order to evaluate the potential applicability of the $\overline{\text{SNR}}$ approach for such cases, simulations with 27 electrodes placed inside a circular hole of a 2D model were performed. Two conductivity contrasts shown in Fig. 11(i) were reconstructed for three different skips using the GN algorithm with identical $\overline{\text{SNR}}$. The computation of $\overline{\text{SNR}}$ was based on 40 targets placed in the close vicinity around the electrodes as shown by red dots in Fig. 11(i).

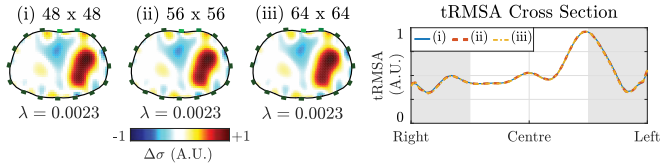

Fig. 6. Noise performance of GN reconstructions (with fixed $\overline{\text{SNR}} = 2.20\text{E-}5$ and a skip of 3) for three examples of image resolution ((i) 48×48, (ii) 56×56, (iii) 64×64). For each resolution we show one single EIT image (all with identical noise), and the corresponding cross sections of the tRMSA images on the right. All images are normalized as described in Fig. 3.

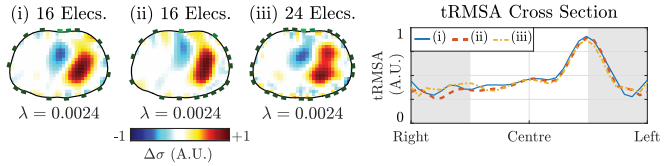

Fig. 7. Noise performance of GN reconstructions (with fixed $\overline{\text{SNR}} = 2.20\text{E-}5$ and a skip of 5) for three examples of varying electrode position and number, where (i) and (ii) have 16 and (iii) 24 non-equidistantly spaced electrodes. For each scenario we show one single EIT image (all with identical noise), and the corresponding cross sections of the tRMSA images on the right. All images are normalized as described in Fig. 3.

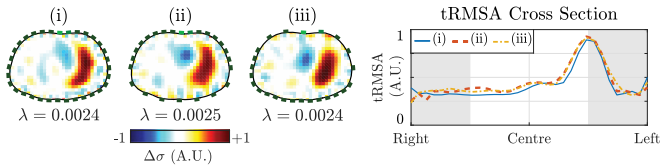

Fig. 8. Noise performance of GN reconstructions (with fixed $\overline{\text{SNR}} = 2.20\text{E-}5$) for three examples of varying electrode position and number, and skip pattern: (i) 32 electrodes with skip 3, (ii) 24 electrodes distributed more ventrally with skip 5 and (iii) 24 electrodes distributed more dorsal with skip 7. For each scenario we show one single EIT image (all with identical noise), and the corresponding cross sections of the tRMSA images on the right. All images are normalized as described in Fig. 3.

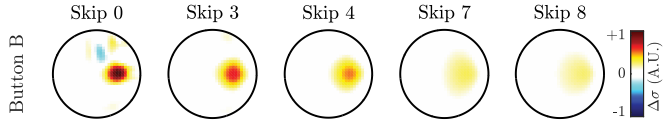

Fig. 9. Conductivity changes $\Delta\sigma$ measured on a resistor phantom for five different skip patterns and reconstructed using GREIT with a fixed noise figure ($\text{NF} = 0.5$). Pressing button B on the phantom leads to a local conductivity perturbation close to electrode 9 (right of image). This perturbation is identical for all skip patterns, such that differences in the resulting images can be attributed to differences in image reconstruction. All images are normalized identically to the maximal absolute amplitude of all five images.

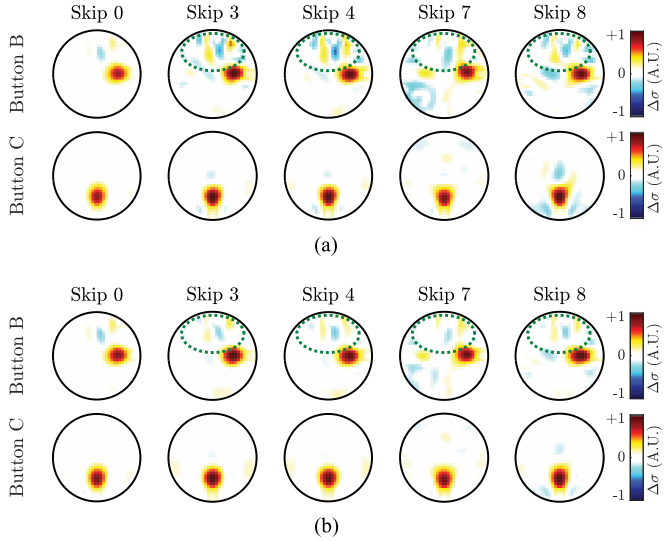

Fig. 10. Conductivity changes $\Delta\sigma$ measured on a resistor phantom for five different skip patterns. Pressing button B and C on the phantom leads to a local conductivity perturbation close to electrode 9 (right of image) and electrode 17 (bottom of image), respectively. The images were reconstructed using GREIT with a fixed $\overline{\text{SNR}}$ of (a) $\overline{\text{SNR}}_1 = 3.22\text{E-}6$ or (b) $\overline{\text{SNR}}_2 = 5.16\text{E-}3$, both corresponding to a $\text{NF} = 0.5$ at skip 0. The difference in $\overline{\text{SNR}}$ between (a) and (b) is due to the different noise covariances used: (a) $\boldsymbol{\Sigma}_n = \boldsymbol{I}$ or (b) $\boldsymbol{\Sigma}_n = \boldsymbol{\Sigma}_{\text{Est}}$. The green dotted ellipses highlight the zone where differences in image artefacts are observed. All images in one row are normalized identically to the maximal absolute amplitude of all five images.

III. Results

A. Simulation Experiments

Figs. 4–8 show the noise performance of different scenarios and hyperparameter selection approaches resulting from the simulation experiments illustrated in Fig. 3.

Fig. 4 shows the noise performance of GN reconstructions for four examples of skip patterns and for different hyperparameter selection approaches: (a) a fixed noise figure ($\text{NF} = 0.5$), (b) GCV, (c) LCC, (d) a fixed $\overline{\text{SNR}}$ of $\overline{\text{SNR}}_1 = 2.20\text{E-}5$, and (e) a two-fold higher $\overline{\text{SNR}}_2 = 4.41\text{E-}5$.

Similar figures are shown for an identical $\overline{\text{SNR}}_1$ to depict how the noise performance as influenced by: (a) the use of the GREIT – instead of GN – reconstruction algorithm (see Fig. 5), (b) different image resolutions (Fig. 6), (c) varying electrode position and number (see Fig. 7), and finally, (d) different skips combined with varying electrode position and number (see Fig. 8).

All images in Figs. 4–8 are normalized to the maximal tRMSA (as illustrated in Fig. 3). The reason behind this normalization is that – independent of differences in amplitude response of reconstruction – we would like to display and analyze differences in NP and thus the ratio of signal level at each pixel relative to the maximal noise-affected signal level.

B. Practical Experiments

Fig. 9 depicts EIT images of an identical conductivity change measured on a resistor phantom for five different skip patterns and reconstructed using a n algorithm with a fixed NF.

Similar images reconstructed with a fixed $\overline{\text{SNR}}$ are shown in Fig. 10(a). As per default, the calculation of $\overline{\text{SNR}}$ for these images is based on (10) with $\sigma_n = 1$. In contrast, images in Fig. 10(b) show the effect of taking into account the

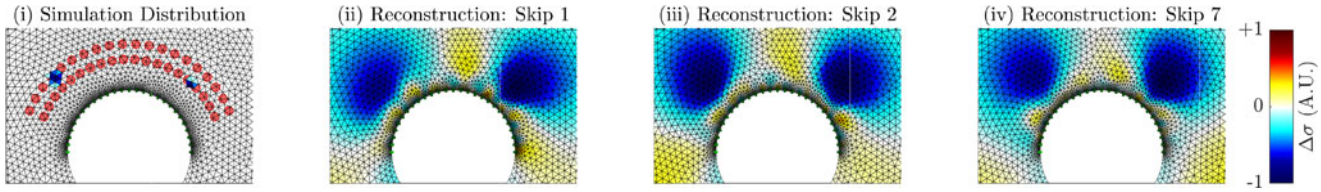

Fig. 11. Example of 27 electrodes placed inside an open geometry. (i) Shows the $n_t = 40$ targets used to calculate the $\overline{\text{SNR}}$ (red dots) and the two conductivity changes simulated (bluish elements) which were reconstructed with GN algorithms having an identical $\overline{\text{SNR}}$ for three different skips: (ii) 1, (iii) 2 and (iv) 7. The images of the reconstructed conductivity changes $\Delta\sigma$ in (ii)–(iv) are normalized to the maximal absolute amplitude of all three images.

device-inherent noise characteristics ($\overline{\text{SNR}}$ calculation is based on (9), with $\mathbf{\Sigma}_n$ equal to the estimated noise covariance $\mathbf{\Sigma}_{\text{Est}}$).

C. Open Geometry Example

Fig. 11 (ii)–(iv) shows images of the open geometry conductivity change reconstructed for three different skip patterns with identical $\overline{\text{SNR}}$ and noise.

IV. Discussion

In this paper we suggest a novel noise performance (NP) metric which allows for a fair comparison of EIT reconstruction algorithms with different measurement configurations (i.e. skip pattern, number and position of electrodes, etc.). We validated its applicability based on three experiments: 1) simulations on a human thorax model, 2) practical measurements on a resistor phantom, and 3) simulation of an open geometry example. The results obtained are discussed in detail hereafter.

A. Simulation Experiments

Fig. 4(a) reveals that the NF approach leads to a very inhomogeneous NP, as the noise level decreases with increasing skip. It thus cannot be used to achieve a similar NP between algorithms with unequal measurement configurations (e.g. different skips). The higher the skip, the more regularized and thus smoothed the result is, when aiming for the same NF. On the other hand, for the GCV [see Fig. 4(b)] a similar NP can be observed among all four skips, with the exception of skip 0 (i) where the noise level is increased by roughly 50%. This is improved with the LCC [see Fig. 4(c)] which shows a more homogeneous NP between all skips. Furthermore one can observe that GCV tends to regularize less (smaller λ, higher noise level), which is a known characteristic [16]. However, the latter two approaches (1) require actual data including noise and (2) can only be applied to reconstruction algorithms using Tikhonov-type regularization, i.e. GN but not GREIT. This is why both do not fulfil our requirements of a versatile NP metric.

In contrast, the selection of λ with the $\overline{\text{SNR}}$ approach results in a comparable NP for both $\overline{\text{SNR}}_1 = 2.20\text{E-}5$ [see Fig. 4(d)] or a two-fold higher $\overline{\text{SNR}}_2 = 4.41\text{E-}5$ [see Fig. 4(e)]. This shows that for the same scenario, the $\overline{\text{SNR}}$ is a robust way to obtain comparable NP between the varying skips. Besides, the NP in the image domain can be flexibly adapted as demonstrated by the two-fold increase in $\overline{\text{SNR}}$ from (d) $\overline{\text{SNR}}_1$ to (e) $\overline{\text{SNR}}_2$ which results in an approximate two-fold increase in NP.

The use of GREIT instead of GN for reconstructing with a fixed $\overline{\text{SNR}}_1$ is shown in Fig. 5 and reveals a spatial distribution of noise different to that of GN [see Fig. 4(d)]. An attenuation of noise close to the model border can be observed for images reconstructed using GREIT, which is known as an inherent property of this algorithm [10]. Nonetheless, the noise level in the ROI - the region in which we evaluate our NP - is closely comparable. This demonstrates the versatility of our approach by its independence on those two commonly used reconstruction algorithms.

Furthermore, the use of different image sizes as shown in Fig. 6 confirms the immunity of the $\overline{\text{SNR}}$ approach to changes in image resolution. In addition, it seems to be robust to differences in electrode placement and number. This is shown in Fig. 7 which depicts the use of non-equidistantly spaced electrodes and a variation in their number for a constant skip of 5. This is extended in Fig. 8 where not only the electrode placement and number, but also the skip is varied. The slightly lower noise level especially for case (i) is a desired behaviour and can be explained by a higher spatial resolution achieved with 32 electrodes, i.e. the same portion of conductivity change is concentrated into a smaller area. As the resulting sum of the normalized impedance change in the TEZ (the signal level S) is lower for 32 electrodes, we also have a lower noise level to achieve the same SNR.

The tRMSA cross section plots confirm that the NP of the different scenarios shown in Fig. 4(d) and Figs. 5–8 closely resemble each other. These simulation results highlight the flexibility of the $\overline{\text{SNR}}$ approach in the example of thoracic EIT and corroborate the use of $\overline{\text{SNR}}$ as valuable NP metric by fulfilling the requirements of being insensitive to the 1) measurement configuration (skip, electrode number and position), 2) image resolution and 3) reconstruction algorithm.

B. Practical Experiments

The aforementioned problems with a fixed NF, are confirmed in experimental measurements as shown in Fig. 9. These images show an increase in spatial blurring and a corresponding decrease in noise level with increasing skip. Besides, one can observe a decrease in conductivity change which is due to an increase in regularization with increasing skip. A possible solution is given by the $\overline{\text{SNR}}$ approach as depicted in Fig. 10(a), where, independent of the skip, a similar NP is achieved.

However, for a conductivity change at the right of the image (button B), artefacts can be observed (green dotted zone). These are present for a skip other than 0 and primarily located at the top of the images, which corresponds to the vicinity of electrode 1. We presume that these specific artefacts are an inherent property of the device used, as it was already reported previously in [17]. When considering the device-specific noise characteristics $\mathbf{\Sigma}_{\text{Est}}$ by using (9) for the $\overline{\text{SNR}}$ calculation, these artefacts are reduced and the images in Fig. 10(b) still show a comparable NP. This points out that real EIT data are very likely to not have purely uniform noise among all channels [18]. At the same time these results underline the versatility of the $\overline{\text{SNR}}$ approach to incorporate the device-specific noise characteristics in order to calculate more realistic NPs.

In practice, for thoracic EIT measurements, we may predetermine the noise characteristics of our device in the lab (e.g. on a resistor phantom) and later include this information to tune the algorithm before applying it to image living beings.

C. Open Geometry Example

The images of the open geometry example [see Fig. 11 (ii)–(iv)] show a visually comparable NP. This simple example lets us assume that our approach has the potential to be used for such applications of EIT. However, further investigations in this particular field are required, e.g. regarding the selection of application-specific algorithm parameters (ROI, target size and position, etc.).

D. Algorithm Parameter Selection

The $\overline{\text{SNR}}$ calculation depends on several parameters (ROI, n_t, r_t, $\mathbf{\Sigma}_n$) which are discussed and justified in the following.

1) ROI: In thoracic EIT we are primarily interested in respiration- or cardiovascular-induced conductivity changes. It thus makes sense to have an ROI in the centre which covers big parts of the lungs and heart as also shown in Fig. 3(b). Depending on the application, this ROI should be moved to the region(s) where conductivity changes of interest are most likely to be observed and analysed.

2) Targets: The number of targets n_t uniformly distributed inside the ROI is chosen high enough to achieve a homogeneous estimate of NP over the entire region. However, a higher n_t leads to increased computation time which explains the suggested value of $n_t = 200$ as compromise. The relative target radius r_t with 5% of the model diameter is justified with being inferior to the inherent spatial resolution of EIT with 32 electrodes [19], [20].

3) The Ideal $\overline{\text{SNR}}$ Value: Even tough the $\overline{\text{SNR}}$ value allows a fair comparison between different measurement configurations, its absolute value still is related to the noise characteristic ($\mathbf{\Sigma}_n$) and thus depends on factors influencing the voltage amplitude such as drive current, amplification gain, etc. Therefore we cannot recommend a specific range of $\overline{\text{SNR}}$ values as ideal for clinical EIT applications. Nevertheless, we suggest to set $\overline{\text{SNR}}$ such that it corresponds to a NF in the range of 0.5–2 (necessarily calculated for 16 equidistantly spaced electrodes with *adjacent* stimulation, i.e. skip 0) as suggested in [5].

E. Limitations and Future Work

In the present study we only consider the use of one-step linearised reconstruction algorithms. Nevertheless, the approach could be extended for other reconstructions – by estimating the noise response of the algorithm by means of Monte Carlo simulations – with the drawback of significantly increased computation time.

Furthermore, we restrict the induced disturbances to additive noise, even though there is evidence that this is not always appropriate for real EIT data [18], [21]. This choice is mainly justified to facilitate statistical computations and allow for an analytic and thus computationally efficient solution. Moreover, this does not represent a drawback from the current state of the art, as the NF relies on the same assumption. However, more sophisticated noise models could be taken into account when using Monte Carlo simulations.

Despite the three dimensional nature of the EIT problem and the consequent need for 3D reconstruction [22], almost all clinical chest EIT is measured and reconstructed in 2D [3]. For this reason the analysis in this paper was also restricted to 2D EIT imaging. However, the $\overline{\text{SNR}}$ approach could be used for 3D EIT without significant modifications. In this case, the TEZ would automatically be adapted – via the one-fourth amplitude threshold – to a spherically-shaped region containing the voxels of interest.

Moreover, the current implementation estimates the $\overline{\text{SNR}}$ from spherical targets with uniform conductivity change. However, the lung, the heart or other (parts of) anatomical structures representing more realistic conductivity changes might be better suited targets and therefore explored in the future. The introduction of targets with different shapes and conductivity changes should not be an issue. The only modification necessary would be to normalize each signal estimate S by a correction factor incorporating the relative change in conductivity $\Delta\sigma/\sigma_r$ of each target [10].

V. Conclusion

In summary, this paper has developed a new measure of noise performance ($\overline{\text{SNR}}$), which permits comparison of EIT reconstruction performance across different measurement configurations. Results are validated by simulations and phantom measurements. This measure offers advantages over current approaches (NF, LCC, GCV), as it is independent of 1) measurement configuration (skip, electrode number and position), 2) image resolution and 3) reconstruction algorithm.

References

[1] I. Frerichs *et al.*, "Chest electrical impedance tomography examination, data analysis, terminology, clinical use and recommendations: Consensus statement of the translational eit development study group," *Thorax*, vol. 72, no. 1, pp. 83–93, 2016.

[2] D. S. Holder, *Electrical Impedance Tomography: Methods, History and Applications*. Bristol, U.K.: Institute of Physics, 2005.

[3] A. Adler *et al.*, "Whither lung EIT: Where are we, where do we want to go and what do we need to get there?" *Physiol. Meas.*, vol. 33, no. 5, pp. 679–694, 2012.

[4] W. R. B. Lionheart, "EIT reconstruction algorithms: Pitfalls, challenges and recent developments," *Physiol. Meas.*, vol. 25, no. 1, pp. 125–142, 2004.
[5] B. M. Graham and A. Adler, "Objective selection of hyperparameter for EIT," *Physiol. Meas.*, vol. 27, no. 5, p. S65–79, 2006.
[6] T. Correia *et al.*, "Selection of regularization parameter for optical topography," *J. Biomed. Opt.*, vol. 14, no. 3, 2009, Art. no. 034044.
[7] P. C. Hansen and D. P. O'Leary, "The use of the L-curve in the regularization of discrete III-posed problems," *SIAM J. Sci. Comput.*, vol. 14, no. 6, pp. 1487–1503, 1993.
[8] G. H. Golub, M. Heath, and G. Wahba, "Generalized cross-validation as a method for choosing a good ridge parameter," *Technometrics*, vol. 21, no. 2, pp. 215–223, 1979.
[9] A. Adler and R. Guardo, "Electrical impedance tomography: Regularized imaging and contrast detection," *IEEE Trans. Med. Imag.*, vol. 15, no. 2, pp. 170–179, Apr. 1996.
[10] A. Adler *et al.*, "GREIT: A unified approach to 2D linear EIT reconstruction of lung images," *Physiol. Meas.*, vol. 30, no. 6, pp. S35–55, 2009.
[11] A. Adler and W. Lionheart, "Uses and abuses of EIDORS: An extensible software base for EIT," *Physiol. Meas.*, vol. 27, no. 5, pp. S25–42, 2006.
[12] P. A. Hasgall *et al.*, "IT'IS Database for thermal and electromagnetic parameters of biological tissues," Sep. 2015. [Online]. Available: http://dx.doi.org/10.13099/VIP21000-03-0
[13] P. C. Hansen, *Rank-Deficient and Discrete Ill-Posed Problems: Numerical Aspects of Linear Inversion*. SIAM, 1998.
[14] P. C. Hansen, "Regularization tools version 4.0 for Matlab 7.3," *Numer. Algorithms*, vol. 46, no. 2, pp. 189–194, 2007.
[15] Swisstom, *Swisstom Resistor Mesh Phantom User Manual 1ST504-103*, Landquart, Switzerland, Jun. 2013.
[16] L. Tenorio, "Statistical regularization of inverse problems," *SIAM Rev.*, vol. 43, no. 2, pp. 347–366, 2001.
[17] P. O. Gaggero, A. Adler, and B. Grychtol, "Using real data to train GREIT improves image quality," in *Proc. Electro/Inf. Technol. Conf.*, Gananoque, ON, Canada, 2014, p. 27.
[18] G. Hahn *et al.*, "Systematic errors of EIT systems determined by easily-scalable resistive phantoms," *Physiol. Meas.*, vol. 29, no. 6, pp. S163–S172, Jun. 2008.
[19] J. L. Wheeler, W. Wang, and M. Tang, "A comparison of methods for measurement of spatial resolution in two-dimensional circular EIT images," *Physiol. Meas.*, vol. 23, no. 1, pp. 169–176, 2002.
[20] A. Seagar, D. Barber, and B. Brown, "Theoretical limits to sensitivity and resolution in impedance imaging," *Clin. Phys. Physiol. Meas.*, vol. 8, Suppl A, pp. 13–31, 1987.
[21] A. R. Frangi *et al.*, "Propagation of measurement noise through backprojection reconstruction in electrical impedance tomography," *IEEE Trans. Med. Imag.*, vol. 21, no. 6, pp. 566–578, Jun. 2002.
[22] B. H. Brown, "Medical impedance tomography and process impedance tomography: A brief review," *Meas. Sci. Technol.*, vol. 12, no. 8, pp. 991–996, 2001.

Authors' photographs and biographies not available at the time of publication.